Post-heat treatment pressure effect on performances of metal-supported solid oxide fuel cells fabricated by atmospheric plasma spraying

Chun-Huang Tsai, Chang-sing Hwang*, Chun-Liang Chang, Jen-Feng Yu, Sheng-Hui Nien

Physics Division, Institute of Nuclear Energy Research, Lungtan, Taoyuan 32546, Taiwan, ROC

ABSTRACT

The nickel metal-supported cells fabricated by atmospheric plasma spraying are post-heat treated in air at 960 °C for 2 h with different pressures. The current–voltage–power and AC impedance measurements show the prepared cell with an applied pressure of 450 g cm^{-2} in the post-heat treatment has a better electrochemical performance at test temperatures ≥ 650 °C. For test temperatures < 650 °C, the maximum power densities at 450 g cm^{-2} pressure are about the same as the maximum power densities at 1250 g cm^{-2} pressure. The SEM micrograph indicates that the cathode including the cathode interlayer and the cathode collector is the most porous region in the cell. AC impedance results show this cathode is the most sensitive part to the applied pressure in the post-heat treatment and the cell with 450 g cm^{-2} pressure has the smallest low frequency intercept R_2 and the polarization resistance R_p at temperatures from 600 to 800 °C. The performance durability test of the cell post-heat treated at 450 g cm^{-2} pressure shows a degradation rate of 0.0087 mV h^{-1} or 0.0026 mW h^{-1} at 300 mA cm^{-2} constant current density and 750 °C test temperature.

1. Introduction

The solid oxide fuel cell (SOFC) is an electrochemical reactor for generating electricity and has some unique advantages over the traditional power generation technologies, including inherently high efficiency, low gas pollution emissions and fuel flexibility [1–3]. Over the past two decades, technical developments have focused on the development of both advanced SOFC materials and structures so that the reduction of cell operation temperature can be realized [4–8]. SOFCs with reduced operation temperature (600–800 °C) provide numerous advantages such as wider choices of low-cost component materials, improved sealing and interfacial reaction prevention, and increased flexibility in the structure design [9–11].

In the development of reduced temperature SOFC technology, reducing electrolyte thickness and developing alternative materials with high ion conductivity at reduced temperatures are two major approaches to minimize the energy loss from electrolyte. The LSGM has been reported as a material with higher ion conductivity than YSZ material and chosen as a good electrolyte for intermediate temperature solid oxide fuel cells (ITSOFCs) [12,13]. There is also a tendency to shift ceramic-supported fuel cells to metal-supported fuel cells toward lowing operation temperatures, due to

the potential benefits of low cost, high strength, better workability, good thermal conductivity and quicker start-up [14,15]. Quicker start-up and thermal cycling are considered as the main causes of ceramic-supported fuel cell breakage and stack failure [16,17]. Metal-supported fuel cells are desired to be used in the auxiliary power unit of mobile application where the structural robustness and the thermal shock resistance with low internal temperature and stress gradients are required [18,19]. In addition, the use of metallic substrates allows the use of conventional metal welding techniques for stack sealing and could significantly reduce the manufacturing costs of SOFC stacks.

The atmospheric plasma spraying (APS) that is well known in the industrial applications is a part of thermal spraying, a group of processes in which metallic and non-metallic powders are deposited in a molten or semi-molten state on a prepared substrate [20,21]. This spraying process shows strong potential to enable the sequential multi-layer depositions of metal-supported fuel cells on preheated porous metallic substrates [22,23]. In our approach, the LSGM (La$_{0.8}$Sr$_{0.2}$Ga$_{0.8}$Mg$_{0.2}$O$_{3-\delta}$) material with higher ion conductivity was adopted as an electrolyte in the APS process for obtaining high power density metal-supported ITSOFCs. To mitigate unfavorable residual stresses in a cell prepared by the APS coating processes which is a fast sintering process and can generate stresses in a coating, an annealing process for the whole cell is applied with a pressure for eliminating the unwanted cell warping. Hence, it is important to explore the effect of applied pressure in the post heat treatment of fabricating a cell on the cell performance.

* Corresponding author. Tel.: +886 03 4711400x7311; fax: +886 03 4711408.
E-mail addresses: cshwang@iner.gov.tw, chansin.hwang@msa.hinet.net
(C.-s. Hwang).

Table 1
Typical parameter values of atmospheric plasma spraying.

| Spray parameter	Anode functional layer	Buffer layer	Electrolyte layer	Composite cathode layer	Current collector layer	Unit
Torch power	36–38	42–14	47–19	26–28	26–28	kW
Primary argon flow rate	50–54	50–54	50–54	50–54	50–54	slpm
Secondary helium flow rate	20–25	20–25	20–25	20–25	20–25	slpm
Secondary hydrogen flow rate	6–8	6–8	6–8	2–4	2–4	slpm
Argon carry gas flow rate	3–5	3–5	3–5	3–5	3–5	slpm
Powder feed rate	2–10	2–10	2–10	2–10	2–10	g min^{-1}
Spray distance	95	90	90	95	95	mm
Preheated substrate temperature	500	700	700	500	500	°C
Robot scan speed	600	1000	600	600	600	mm s^{-1}

2. Experiments

The APS system consisted of mainly a modified Praxair SG-100 dc plasma torch with Mach I nozzle that inject a high temperature plasma flame under atmospheric condition, two powder feeder systems for delivering plasma sprayable powders, a cooling system for the torch, a furnace for preheating the substrate, an IR detector for measuring the temperature of the substrate, a fast CCD camera to observe trajectories of particles in the plasma flame and a Fanuc Robot ARC Mate 120iB system to scan plasma torch. The modified Praxair SG-100 dc plasma torch with Mach I nozzle was operated at medium currents from 300 to 460 A and at high voltages from 88 to 105 V. The mixed gas from argon, hydrogen and helium was used as plasma forming gas. A specially designed multi-gas mixer was applied to mix these gases uniformly. Other details of experimental apparatus are given in earlier papers [24,25] and typical plasma spraying parameters are shown in Table 1.

Commercially available powders of LDC ($Ce_{0.55}La_{0.45}O_{2-\delta}$), LDC/NiO, LSCF ($La_{0.58}Sr_{0.4}Co_{0.2}Fe_{0.8}O_{3-\delta}$)/C, and LSGM ($La_{0.8}Sr_{0.2}Ga_{0.8}Mg_{0.2}O_{3-\delta}$) obtained from Inframat, Inc., USA and Specialty Ceramics of Praxair, USA were applied to construct a metal supported solid oxide fuel cells by atmospheric plasma spraying processes. The morphologies of these powders are shown in Fig. 1. LDC, LDC/NiO, LSCF/C and LSGM are agglomerated

powders that have average granule sizes from 20 to 50 μm and can be sprayed directly by APS. Carbon black of 15 wt% is applied as a pore former and it will be burn out during the plasma spray coating. The original particles of LDC and LDC/NiO agglomerated powders are less than 100 nm in size, but the original particles of LSCF agglomerated powders are between 200 nm and 400 nm in size. The Ni content in LDC/NiO powders is about 50% in volume after reduction. The LSGM powders are sieved into a smaller range of powder sizes before plasma spraying. Layers of LDC/NiO, LDC, LSGM, LSGM/LSCF and LSCF were sprayed by APS in sequence on a porous nickel substrate to complete a Ni-LDC/NiO-LDC-LSGM-LSGM/LSCF-LSCF cell. The LSGM/LSCF interlayer is formed of LSGM and LSCF with 50%:50% in volume, this layer is applied for matching gradually the thermal expansion coefficients of dense LSGM electrolyte and porous LSCF layer. The LDC layer is used to inhibit nano nickel particles in the anode to diffuse into LSGM electrolyte and react with LSGM material. To support the whole cells, the nickel substrates with 1.2 mm in thickness are adopted. The NiO can be reduced to Ni by hydrogen gas during the cell test.

The four completed APS cells named as cell A, B, C and D with 1.76 cm^2 active area of LSCF layer for collecting cell current were prepared to study the effect of applied pressure in the post-heat treatment, they were supported by porous nickel substrates with a diameter of 24 mm and a permeability of about 0.5 Darcy. The
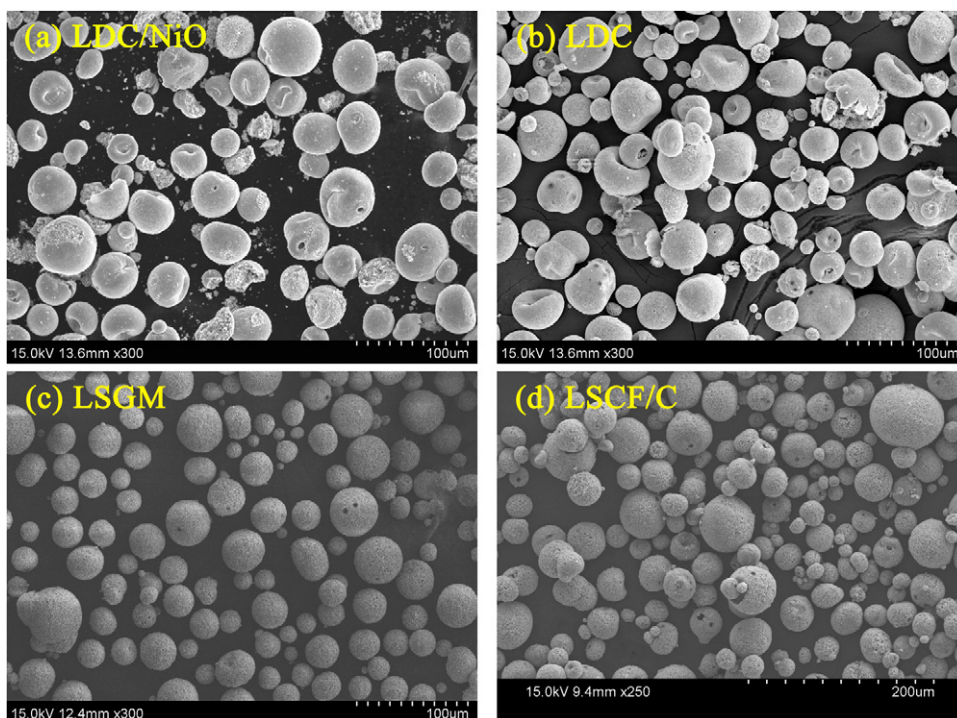
Fig. 1. SEM photos of powders: (a) LDC/NiO, (b) LDC, (c) LSGM and (d) LSCF/C used to fabricate ITSOFCs.
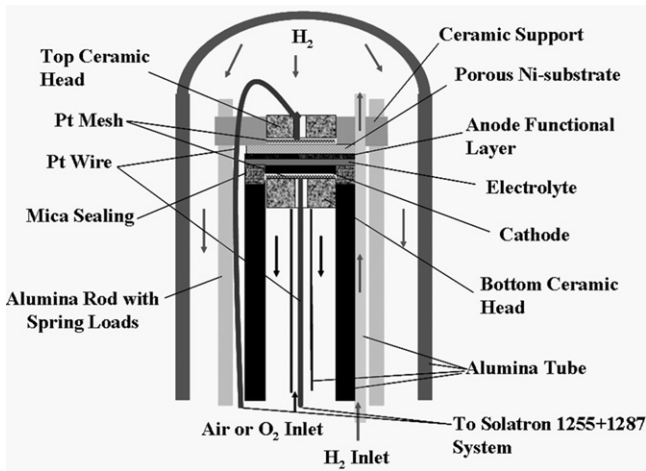
Fig. 2. The scheme of testing APS sprayed cells.

same plasma spray parameters were used to coat these cells. After plasma spray coating, the prepared cells were heated at 960 °C for 2 h in air with different pressures. The applied pressures in the post-heat treatment are 0, 450, 1250 and 10,000 g cm^{-2} for cell A, cell B, cell C and cell D, respectively. These cells have a nano-structured LDC/Ni anode functional layer and an LDC interlayer, an LSGM electrolyte layer, an LSGM/LSCF cathode interlayer and an LSCF cathode current collector layer. Before these cells were measured in a modified ProboStat measurement system with Solartron 1255 and 1287 units for power and AC impedance measurements, a silver net which covered about 50% active area of LSCF current collector was printed on the LSCF layer of each cell to minimize the cathode contact resistance. Platinum meshes and wires were used for collecting and transporting anode and cathode currents. In the AC impedance measurement, a 10 mV AC signal with frequencies from 0.1 to 1 MHz is applied to the cell operated at OCV (open circuit voltage) condition. The prepared button cell was sealed onto one open end of an inner alumina tube by mica, glass sealers and spring load. After the reduction of the NiO anode in H$_2$ for several
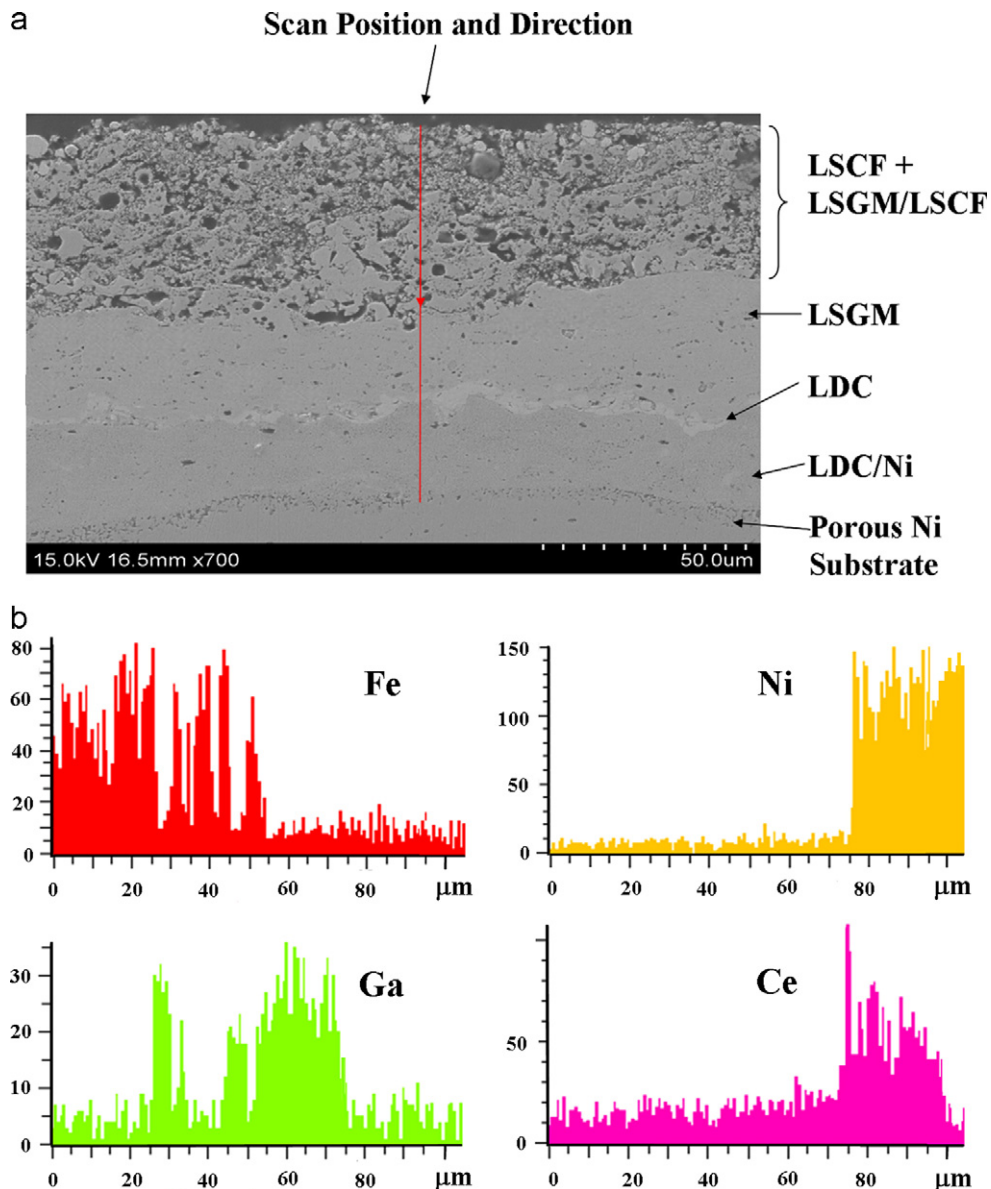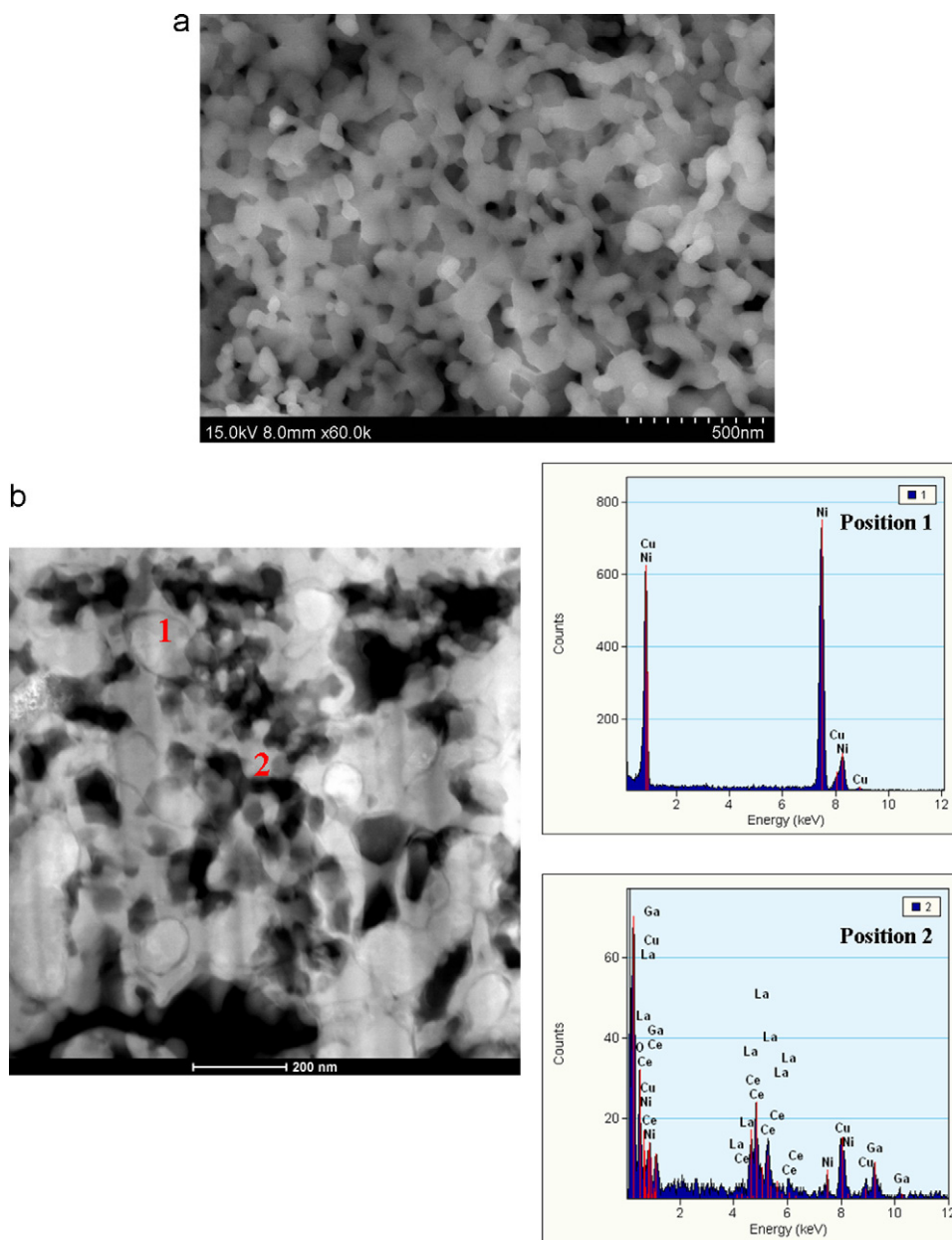

Fig. 3. (a) Cross sectional SEM micrograph of an APS prepared cell B after cell test. (b) EDX line mappings of elements along the selected scan position and direction as shown in (a).

Fig. 4. (a) Cross sectional SEM micrograph of nanostructured LDC/Ni anode in a high magnification. (b) TEM image of this nanostructured LDC/Ni anode in high magnification and corresponding EDX signals at position 1 and 2.

hours, the performances of the cell were measured at various temperatures from 600 to 800 °C. The scheme for measuring output power densities and AC impedances of APS plasma sprayed cells is shown in Fig. 2. The flow rates of hydrogen fuel and oxygen oxidizer were kept as 300 ml min^{-1} in these measurements. For the long term durability measurement, one additional cell supported by the same porous nickel substrate with a diameter of 50 mm was prepared by the same APS processes and post heat treatment condition as those applied for the cell B. This prepared cell had a 15 cm^2 active area of LSCF layer for collecting cell current and for the simplicity of without the aging effect of mica seal, it was measured in a non-seal cell test housing under 335 ml min^{-1} hydrogen fuel and 670 ml min^{-1} air oxidizer flow rates. The details of this non-seal cell test housing were described in the earlier paper [26]. The microstructures and EDX signals of APS cells prepared in this work were analyzed via SEM (Hitachi S4800) and TEM (FEI Tecnai^{TM} G2 F-20) microscopes.

3. Results and discussion

3.1. Microstructures

A typical microstructure of an APS prepared cell B after cell test is shown in Fig. 3a. Multi-functional layers of this cell were deposited on the porous nickel substrate by atmospheric plasma spraying processes. As shown in Fig. 3a, the LSGM layer is found to be quite dense with closed pores and without cracking through. Good interfacial adhesion is found between different functional layers of a cell. Fig. 3b gives the EDX line mappings of elements along the selected scan position and direction shown in Fig. 3a, the EDX signals of key elements Fe, Ni, Ga, Ce versus thickness are given in this figure. The scan direction of line mapping is from cathode to nickel substrate. The thicknesses of different layers shown in Fig. 3b along the selected scan position and direction can be estimated by the EDX signals of these key elements. The EDX signal of
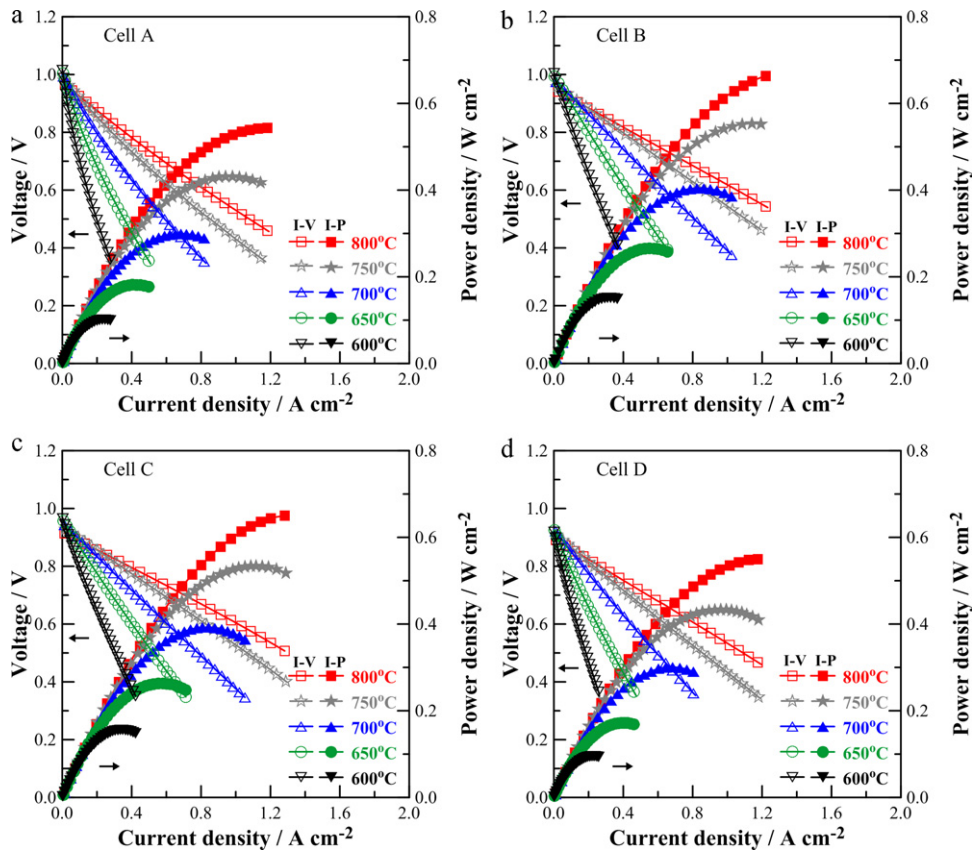
Fig. 5. Measured *I–V–P* results of cell A, cell B, Cell C and cell D at temperatures of 600, 650, 700, 750 and 800 °C.

Fe element at about 53 μm is used to calculate the total thickness of LSGM/LSCF cathode interlayer plus LSCF current collecting layer, this estimated thickness is around 53 μm. The difference of EDX signal of Fe element at about 53 μm and EDX signal of Ga element at about 74 μm is used to estimate the LSGM electrolyte thickness which is around 21 μm. The difference between Ce element EDX signal at about 74 μm and Ni element EDX signal at about 76 μm is used to estimate the LDC interlayer thickness which is around 2 μm. The difference between Ni element EDX signal at about 76 μm and Ce element EDX signal at about 99 μm is used to estimate the thickness of LDC/Ni anode functional layer which is about 23 μm. Fig. 4a gives the SEM image of nanostructured LDC/Ni anode in a high magnification. The TEM image of this nanostructured LDC/Ni anode in high magnification and corresponding EDX signals at position 1 and 2 are given in Fig. 4b. The EDX signals of Cu and Ga elements in Fig. 4b are believed to come from processes for preparing the TEM sample. The gallium ion beam was applied in this FIB milling method and the copper mesh was used to support the TEM sample. These EDX signals indicate that a nano Ni particle is at the position 1 and a cluster of nano Ni particles and nano LDC particles is at the position 2. This anode contains nano pores, pores larger than 100 nm, nano Ni particles, nano LDC particles and clusters formed by nano Ni particles and nano LDC particles.

3.2. Pressure effect of post-heat treatment on cell performances

Measured *I–V–P* (current–voltage–power) results of cell A, cell B, cell C and cell D at temperatures of 600, 650, 700, 750 and 800 °C are shown in Fig. 5. The hydrogen fuel with 300 ml min^{-1} and the oxygen oxidizer with 300 ml min^{-1} are supplied to the all tested cells. The cell B has a better *I–V–P* performance at all test temperatures except 600 °C, it delivers 0.152, 0.205, 0.404, 0.553, and 0.665 W cm^{-2} maximum output power densities at 600, 650, 700, 750 and 800 °C, respectively. The measured maximum power densities at 600, 650, 700, 750 and 800 °C versus applied pressures in the post-heat treatment are given in Fig. 6. This figure shows that there is a slow variation of maximum power densities between 450 and 1250 g cm^{-2} pressures. For temperatures $\geq$ 650 °C, the
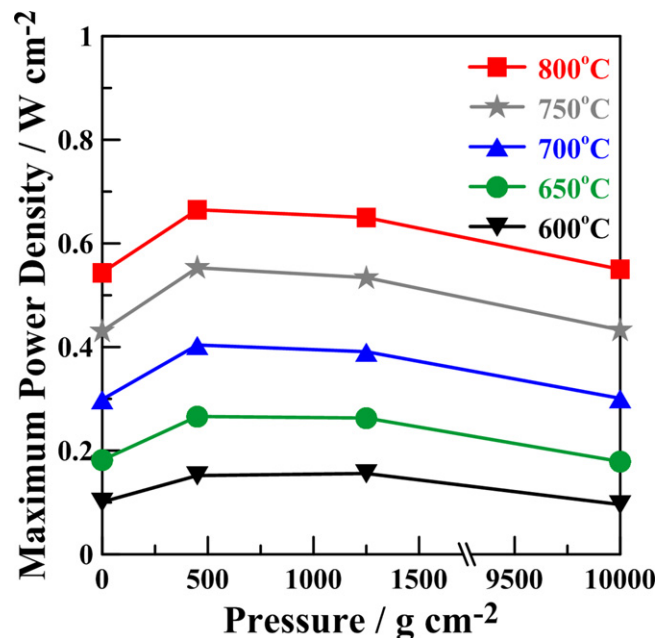

Fig. 6. Measured maximum power densities at 600, 650, 700, 750 and 800 °C versus pressures.
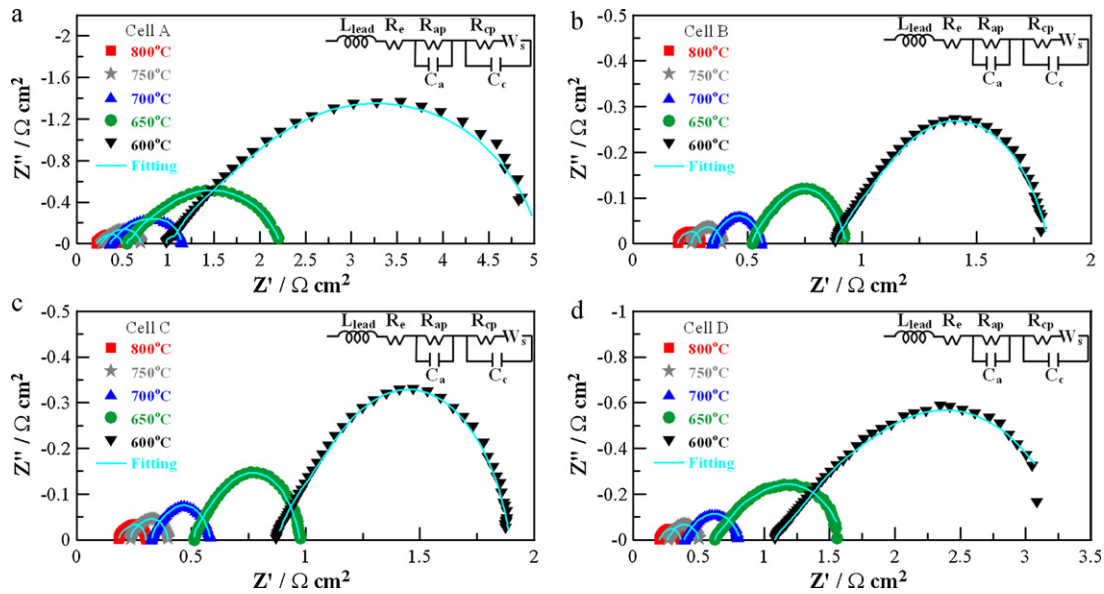
Fig. 7. Cole–Cole plots of AC impedance results measured at the OCV condition for cell A, cell B, cell C and cell D at 600, 650, 700, 750 and 800 °C.

maximum power density at $450\,\mathrm{g\,cm^{-2}}$ pressure is larger than those at other pressures. For temperatures $< 650\,^{\circ}\mathrm{C}$, the maximum power density at $450\,\mathrm{g\,cm^{-2}}$ pressure is about the same as the maximum power density at $1250\,\mathrm{g\,cm^{-2}}$ pressure. The OCV of cell A at $800\,^{\circ}\mathrm{C}$ without pressure in the post-heat treatment is less than 1 V. There are two possible reasons, one is a small leakage through the connected pores in this APS prepared LSGM electrolyte with a thickness of 20–30 μm and the other is the dense nanostructured LDC/Ni anode layer with a thickness of 20–30 μm can reduce the hydrogen pressure at the interface between LSGM electrolyte and nanostructured LDC/Ni anode. The open-circuit voltages larger than 1 V were obtained for APS prepared cells by both increasing the thickness of LSGM electrolyte to 40–50 μm and decreasing the thickness of nanostructured LDC/Ni anode to ~10 μm [24,26]. It is also found that OCVs of tested cells decrease as the applied pressure in the post-heat treatment increases. As shown in Fig. 3a, the cathode (LSCF–LSGM/LSCF) is the most porous layer of the cell and is coated by the plasma spray power of 27–28 kW that is the smallest power among the powers used in the APS fabrication processes of cell. Therefore, it is believed that the cathode including LSGM/LSCF and LSCF layers is the weakest region in the cell and the most sensitive to the applied pressure, then, the decrease of open circuit voltages of cells with pressure is explained by the fact that the porous cathode pressed by a pressure has a denser microstructure unfavorable to the oxygen diffusion and reduction. As the pressure increases, the oxygen pressure at the cathode side interface of LSGM electrolyte is getting smaller and the open circuit voltage decreases.

The Cole–Cole plots of AC impedance results measured at the OCV condition for cell A, cell B, cell C and cell D at 600, 650, 700, 750 and 800 °C are given Fig. 7. Because the imaginary parts of AC impedances cannot consume the energy, only the real parts of AC impedances is interested and discussed. The cell that has a larger real part of AC impedance (cell internal resistance) will deliver less power to the external load. The corresponding real part R_1, R_2 and R_p values of measured AC impedance curves are shown in Table 2. Here, R_1 and R_2 are the high frequency and low frequency intercepts of AC impedance curves on Z' real axis, R_p called as the total polarization resistance is the difference between R_2 and R_1 [1,27,28]. R_1 includes the contact and lead resistances that are kept as small as possible. The simplified equivalent circuit of lumped elements L_{lead}, R_e, R_{ap}, R_{cp}, C_a, C_c and W_s as shown in Fig. 7 is applied to analyze the AC impedance curves. The fitting curves generated by this simplified equivalent circuit are also given in this figure. The fitting curves match the experimental data very well with a fitting χ^2 error about 10^{-4}. In this simplified equivalent circuit, L_{lead} is the lead inductance, R_e is the electrolyte ohmic resistance, R_{ap} is the polarization resistance of anode, R_{cp} is the polarization resistance of cathode, C_a represents the polarization capacitance of anode, C_c represents the polarization capacitance of cathode and W_s is the finite length Warburg short circuit terminus that simulates oxygen oxidant mass transport-diffusion process in the cathode [24,26]. The impedance $Z_{ws}(\omega)$ of finite length Warburg short circuit terminus W_s can be expressed by the following equation:

$$Z_{ws}(\omega) = \frac{W_{s-r} \times \tanh([i \times W_{s-t} \times \omega]^{W_{s-p}})}{(i \times W_{s-t} \times \omega)^{W_{s-p}}} \quad (1)$$

where ω is the frequency, $i = \sqrt{-1}$, W_{s-t} and W_{s-p} are dimensionless fitting parameters, and W_{s-r} is the fitting parameter in $\Omega\,\mathrm{cm^2}$ unit [24,26,29]. As ω approaches to zero, $Z_{ws}(\omega)$ approaches to W_{s-r}. In this simplified equivalent circuit model, the layers of LSGM/LSCF and LSCF are combined together and assumed to act as a cathode that is simulated by R_{cp}, C_c and W_s lumped elements. The layers of LSGM and LDC are combined together and assumed to act as an electrolyte that is simulated by R_e lumped element. The layer of LDC/Ni acting as an anode is simulated by R_{ap} and C_a lumped elements. The resistance of nickel substrate is neglected in this model. Because the anode reaction kinetics is fast compared to the cathode reaction kinetics, the mass transport and diffusion of hydrogen in the nickel substrate and anode are not simulated in this simplified equivalent circuit model.

The obtained values of interested fitting parameters applied in the simplified equivalent circuit are also given in Table 2. According to the simplified equivalent circuit, the low frequency intercept R_2 ($\omega \rightarrow$ zero) $\approx R_e + R_{ap} + R_{cp} + W_{s-r}$ (total internal resistance of cell), the high frequency intercept R_1 ($\omega \rightarrow \infty$) $\approx R_e$ and the total polarization resistance $R_p \approx R_{ap} + R_{cp} + W_{s-r}$ are found. The cathode polarization resistance $R_{cp} + W_{s-r}$ is significantly larger than the anode polarization resistance R_{ap}, this indicates that the cathode contributes the major polarization loss. The variations of R_p, R_1 and R_2 versus pressure at 600, 650, 700, 750 and 800 °C are given in Figs. 8–10. The same variation trends of R_p, R_1 and R_2 versus applied pressures in the post-heat treatment are observed, but R_p has a more significant change with pressures than R_1 does, this is consistent with the above mentioned description that the
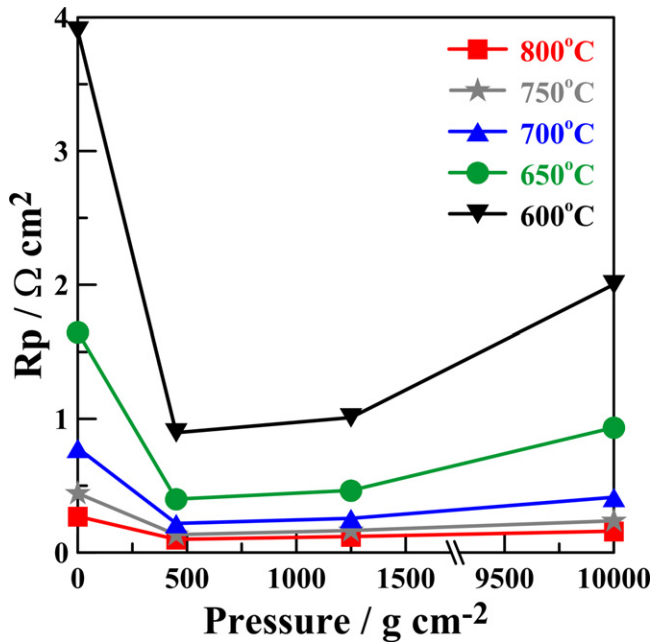
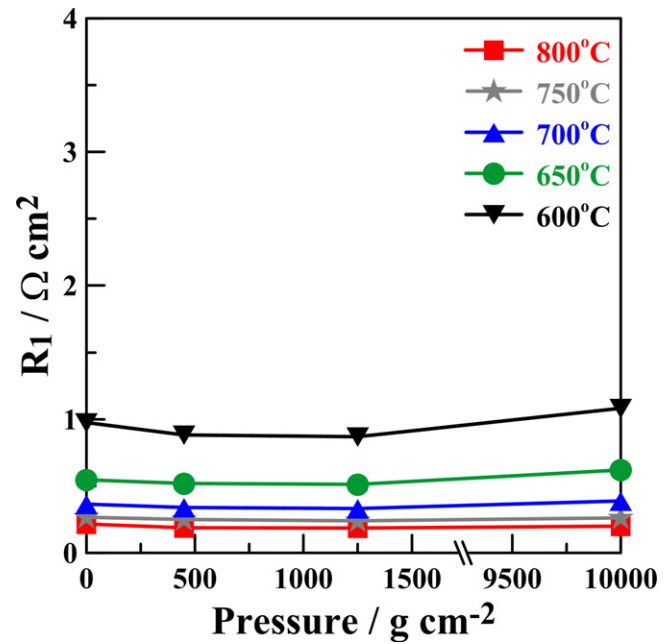**Fig. 8.** R_p versus pressures at 600, 650, 700, 750 and 800 °C.

Fig. 9. R_1 versus pressures at 600, 650, 700, 750 and 800 °C.

cathode is the weakest region in the cell and the most sensitive to the applied pressure in the post-heat treatment. Therefore it is believed that the applied pressure can induce a significant change on the microstructure of the most porous cathode in the cell. When an APS prepared cell is heated at 960 °C for 2 h in air, the adhesions between powders of porous cathode and the adhesion between the cathode and electrolyte get stronger as the applied pressure increases. The porosity of cathode is believed to decrease with the applied pressure. At a small pressure such as 450 g cm^{-2}, the cathode is a little denser (negative effect due to the loss of porosity) and the adhesions (positive effect) mentioned above are greatly better, therefore, among all the tested cells the cell B has a smallest R_2 value as shown in Fig. 10. Qualitatively speaking, the cell with larger OCV can deliver more power than the cell with lower OCV and the cell with lower internal resistance can also deliver more power than the cell with higher internal resistance. Although the OCV of cell B is a little smaller than cell A, but cell B has a significantly small R_2 value than cell A, this implies the cell B has a significantly

lower cell internal resistance than the cell A, hence, the cell B has still the best power performance as shown in Fig. 6. As the applied pressure in the post-heat treatment becomes larger, for instance in the range from 450 to 1250 g cm^{-2} pressure, the positive effect from increased adhesions becomes passivated, the negative effect from loss of porosity that reduces TPB reaction sites in the cathode increases. At the 1250 g cm^{-2} pressure, the negative effect starts to show its significance so that the value of R_2 at this pressure starts to be a little greater than the value of R_2 at the 450 g cm^{-2} pressure. As shown in Fig. 10, the increase rate of R_2 versus pressures applied in the post-heat treatment is small in this pressure range. Due to the lower OCV and higher R_2 of cell C prepared at the 1250 g cm^{-2} pressure, the cell C has a power performance worse than cell B. As the applied pressure begins to be larger than 1250 g cm^{-2}, the negative effect due to the loss of porosity becomes more significant and the TPB reaction sites in the cathode are reduced significantly so that R_p and R_2 values as shown in Figs. 8 and 10 start to increase steeply. Because of lower OCV and higher R_2 of cell D prepared at the

Table 2
The values of R_1, R_2, R_p, R_e, R_{ap}, R_{cp}, W_{s-r} and $R_{cp} + W_{s-r}$ at 600, 650, 700, 750 and 800 °C.

|	Temperature	R_1 (Ω cm^2)	R_2 (Ω cm^2)	R_p (Ω cm^2)	R_e (Ω cm^2)	R_{ap} (Ω cm^2)	R_{cp} (Ω cm^2)	W_{s-r} (Ω cm^2)	$R_{cp} + W_{s-r}$
Cell A (0 g cm^{-2})	800	0.216	0.487	0.271	0.213	0.018	0.004	0.259	0.262
	750	0.267	0.669	0.443	0.263	0.015	0.017	0.411	0.428
	700	0.365	1.147	0.782	0.363	0.028	0.034	0.742	0.776
	650	0.547	2.195	1.648	0.543	0.042	0.035	1.579	1.614
	600	0.976	4.795	3.900	0.976	0.093	0.036	4.000	4.036
Cell B (450 g cm^{-2})	800	0.188	0.287	0.099	0.187	0.009	0.018	0.078	0.096
	750	0.250	0.384	0.134	0.248	0.010	0.020	0.110	0.130
	700	0.340	0.558	0.218	0.340	0.017	0.028	0.177	0.205
	650	0.520	0.920	0.400	0.519	0.024	0.026	0.365	0.391
	600	0.883	1.780	0.897	0.881	0.037	0.028	0.867	0.895
Cell C (1250 g cm^{-2})	800	0.186	0.306	0.120	0.185	0.013	0.020	0.085	0.105
	750	0.240	0.405	0.165	0.236	0.015	0.030	0.118	0.148
	700	0.332	0.588	0.256	0.330	0.018	0.043	0.205	0.248
	650	0.513	0.978	0.465	0.511	0.025	0.045	0.393	0.438
	600	0.870	1.880	1.010	0.869	0.025	0.084	0.901	0.985
Cell D (10,000 g cm^{-2})	800	0.200	0.360	0.160	0.197	0.013	0.020	0.134	0.154
	750	0.262	0.500	0.238	0.257	0.023	0.020	0.185	0.205
	700	0.389	0.803	0.414	0.340	0.029	0.030	0.414	0.444
	650	0.621	1.556	0.935	0.570	0.057	0.031	0.947	0.978
	600	1.083	3.085	2.002	1.020	0.088	0.047	2.181	2.228
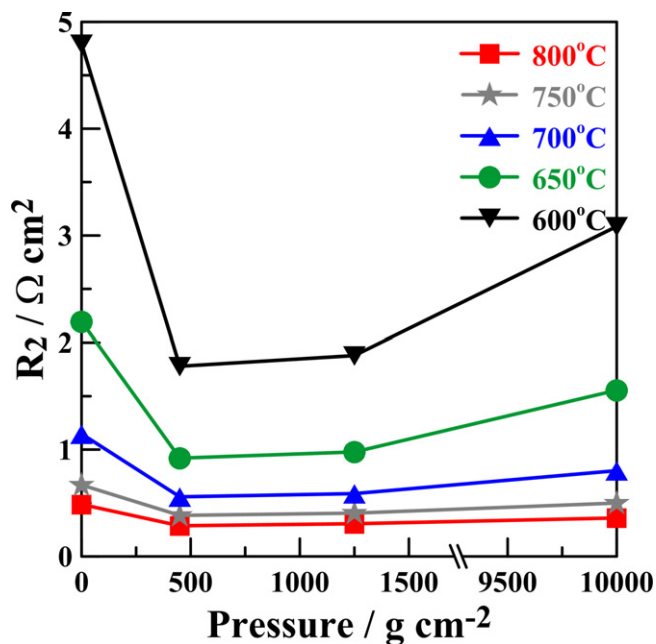
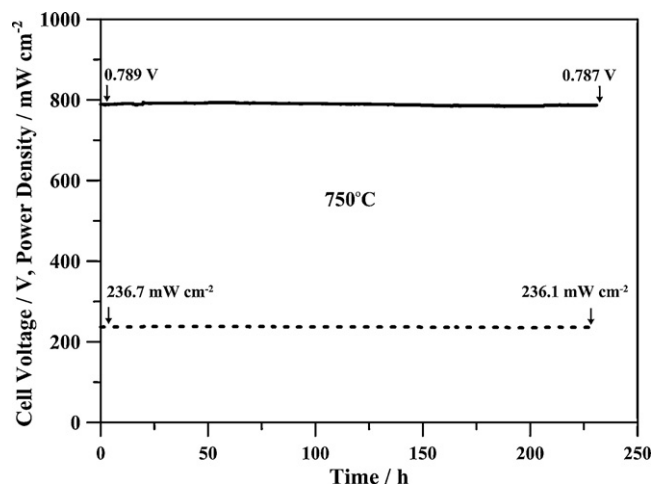**Fig. 10.** R_2 versus pressures at 600, 650, 700, 750 and 800 °C.

Fig. 11. Observed variations of cell voltages and power densities versus time in the durability test at 300 mA cm^{-2} constant current density and 750 °C test temperature.

10,000 g cm^{-2} pressure, the cell D has a worse power performance than cell C.

3.3. Durability test

The cell supported by a porous nickel substrate and having a diameter of 50 mm, a thickness of 1.2 mm and a 15 cm^2 active area of LSCF layer for collecting cell current has been tested in a non-seal cell test housing for a period of 230 h at 300 mA cm^{-2} constant current density and 750 °C test temperature. This cell was prepared by the same APS processes and post heat treatment condition as those applied for the cell B. The corresponding results of measured voltages and power densities versus time are given in Fig. 11. The data shown in Fig. 11 gives the stability of this cell that is post-heat treated at 450 g cm^{-2} pressure. The measured voltage starts from 0.789 V and ends at 0.787 V, and the corresponding measured power density decreases from 236.7 mW cm^{-2} to 236.1 mW cm^{-2}. From the observed variations of voltage and power density shown in Fig. 11, the estimated degradation rate is about 0.0087 mV h^{-1}

or 0.0026 mW h^{-1}. One of probable causes of observed degradation is due to the thermal expansion mismatch between the nickel substrate and LDC/Ni anode functional layer. A high permeable nickel-iron substrate that is expected to have a higher mechanic strength and a better thermal expansion match to LDC/Ni anode functional layer than the porous nickel substrate will be adopted to replace the porous nickel substrate in the future.

4. Conclusions

Four different metal-supported intermediate temperature solid oxide fuel cells with a diameter of 24 mm are prepared by APS technology and are heated at 960 °C for 2 h in air with different pressures. The applied pressures in the post-heat treatment were 0, 450, 1250 and 10,000 g cm^{-2}. These cells have a nano-structured LDC/Ni anode functional layer, an LDC interlayer, an LSGM electrolyte layer, an LSGM/LSCF cathode interlayer and an LSCF cathode current collector layer with 1.76 cm^2 active area. Their performances including power density data and AC impedance results measured at OCV condition versus applied pressures in the post-heat treatment at test temperatures of 600, 650, 700, 750 and 800 °C are studied here. Results show that there is a slow variation of maximum power densities between 450 and 1250 g cm^{-2} pressures. For temperatures ≥ 650 °C, the cell with a pressure of 450 g cm^{-2} has the best power performance among the prepared cells with different pressures. For temperatures < 650 °C, the maximum power densities at 450 g cm^{-2} pressure are about the same as the maximum power densities at 1250 g cm^{-2} pressure. The cell with 450 g cm^{-2} pressure can deliver 0.152, 0.205, 0.404, 0.553 and 0.665 W cm^{-2} maximum power densities at 600, 650, 700, 750 and 800 °C temperatures, respectively. The AC impedance data indicate that the cell polarization resistance R_p is the most sensitive parameter to the variation of applied pressure in the post-heat treatment and the simplified equivalent circuit model analysis shows the cathode polarization resistance $R_{cp} + W_{s-r}$ contributes the major part of R_p. This says that the cathode which is the most porous region in the cell is the most sensitive to the applied pressure. The variations of R_p, R_1 and R_2 versus applied pressures in the post-heat treatment show that there is also a slow variation of these parameters between 450 and 1250 g cm^{-2} pressures and for pressures beyond this range, either less than 450 g cm^{-2} or larger than 1250 g cm^{-2}, a more significant change exists for each of R_p, R_1 and R_2. The cell with applied 450 g cm^{-2} pressure has a cathode microstructure that exhibits the smallest R_p and R_2 values. In the durability test, the results show that the cell post-heat treated at 450 g cm^{-2} pressure has a degradation rate of 0.0087 mV h^{-1} or 0.0026 mW h^{-1} at 300 mA cm^{-2} constant current density and 750 °C test temperature.

References

[1] S.C. Singhal, K. Kendall, High Temperature Solid Oxide Fuel Cell, Elsevier, 2004.
[2] F. Zhao, A.V. Virkar, J. Power Sources 141 (2005) 79–95.
[3] M.C. Williams, J. Strakey, W. Surdoval, J. Power Sources 159 (2006) 1241–1247.
[4] J.P.P. Huijsmans, Curr. Opin. Solid State Mater. Sci. 5 (2001) 317–323.
[5] S.M. Haile, Acta Mater. 51 (2003) 5981–6000.
[6] N.Q. Minh, Solid State Ionics 174 (2004) 271–277.
[7] L. Blum, W.A. Meulenberg, H. Nabielek, R. Steinberger-Wilckens, Int. J. Appl. Ceram. Technol. 2 (6) (2005) 482–492.
[8] W. Gong, S. Gopalan, U.B. Pal, J. Power Sources 160 (2006) 305–315.
[9] K. Föger, J.G. Love, Solid State Ionics 174 (2004) 119–126.
[10] D.J.L. Brett, P. Aguiar, N.P. Brandon, R.N. Bull, R.C. Galloway, G.W. Hayes, K. Lillie, C. Mellors, C. Smith, A.R. Tilley, J. Power Sources 157 (2006) 782–798.

[11] S. Kakaç, A. Pramuanjaroenkij, X.Y. Zhou, Int. J. Hydrogen Energy 32 (2007) 761–786.
[12] F. Bozza, R. Polini, E. Traversa, Electrochem. Commun. 11 (2009) 1680–1683.
[13] R. Vaßen, D. Hathiramani, J. Mertens, V.A.C. Haanappel, I.C. Vinke, Surf. Coat. Technol. 202 (2007) 499–508.
[14] Z. Wang, J.O. Berghaus, S. Yick, C. Decès-Petit, W. Qu, R. Hui, R. Maric, D. Ghosh, J. Power Sources 176 (2008) 90–95.
[15] M.C. Tucker, G.Y. Lau, C.P. Jacobson, L.C. DeJonghe, S.J. Visco, J. Power Sources 175 (2008) 447–451.
[16] C. Lee, J. Bae, J. Power Sources 176 (2008) 62–69.
[17] T. Ishihara, J. Yan, M. Enoki, S. Okada, H. Matsumoto, J. Fuel Cell Sci. Technol. 5 (2008) 031205-1–031205-3.
[18] R. Hui, J.O. Berghaus, C. Decès-Petit, W. Qu, S. Yick, J.-G. Legoux, C. Moreau, J. Power Sources 191 (2009) 371–376.
[19] R. Hui, Z. Wang, O. Kesler, L. Rose, J. Jankovic, S. Yick, R. Maric, D. Ghosh, J. Power Sources 170 (2007) 308–323.
[20] L. Pawlowski, The Science and Engineering of Thermal Spray Coatings, Wiley, New York, 1995.
[21] P. Fauchais, A. Vardelle, B. Dussoubs, J. Therm. Spray Technol. Vol. 10 (2001) 44–66.
[22] R. Henne, J. Therm. Spray Technol. 16 (3) (2007) 381–403.
[23] X.C. Lu, J.H. Zhu, J. Power Sources 165 (2007) 678–684.
[24] C.S. Hwang, C.H. Tsai, C.H. Lo, C.H. Sun, J. Power Sources 180 (2008) 132–142.
[25] C.H. Lo, C.H. Tsai, C.S. Hwang, Int. J. Appl. Ceram. Technol. 6 (4) (2009) 513–524.
[26] C.S. Hwang, C.H. Tsai, J.F. Yu, C.L. Chang, J.M. Lin, Y.H. Shiu, S.W. Cheng, J. Power Sources 196 (2011) 1932–1939.
[27] R.P. O'hayre, S.W. Cha, W. Colella, F.B. Prinz, Fuel Cell Fundamentals, John Wiley & Sons Inc., New York, USA, 2006.
[28] J.W. Fergus, R. Hui, X. Li, D.P. Wilkinson, J. Zhang, Solid Oxide Fuel Cells: Materials Properties and Performance, CRC Press, Boca Raton, FL, USA, 2009.
[29] ZPlot for Windows-Electrochemical Impedance Software Operating Manual, Scribner Associates, Inc., NC, USA, 2000 (Chapter 8).